TU Delft

Delft University of Technology

Document Version
Final published version

Licence
CC BY

Citation (APA)
Liu, Y., van den Berg, R. D., Gijsen, F. J. H., Avril, S., & Akyildiz, A. C. (2026). Material characterization of heterogenous atherosclerotic arteries with the Virtual Fields Method. *Computer Methods and Programs in Biomedicine*, *287*, Article 109642. https://doi.org/10.1016/j.cmpb.2026.109642

Important note
To cite this publication, please use the final published version (if applicable).
Please check the document version above.

Copyright
In case the licence states “Dutch Copyright Act (Article 25fa)”, this publication was made available Green Open Access via the TU Delft Institutional Repository pursuant to Dutch Copyright Act (Article 25fa, the Taverne amendment). This provision does not affect copyright ownership.
Unless copyright is transferred by contract or statute, it remains with the copyright holder.

Sharing and reuse
Other than for strictly personal use, it is not permitted to download, forward or distribute the text or part of it, without the consent of the author(s) and/or copyright holder(s), unless the work is under an open content license such as Creative Commons.

Takedown policy
Please contact us and provide details if you believe this document breaches copyrights.
We will remove access to the work immediately and investigate your claim.

This work is downloaded from Delft University of Technology.

Computer Methods and Programs in Biomedicine 287 (2026) 109642

Contents lists available at ScienceDirect

Computer Methods and Programs in Biomedicine

journal homepage: https://www.sciencedirect.com/journal/computer-methods-and-programs-in-biomedicine

Material characterization of heterogenous atherosclerotic arteries with the Virtual Fields Method

Yanjing Liu [a], Ronald D. van den Berg [b], Frank J.H. Gijsen [a,b], Stéphane Avril [c], Ali C. Akyildiz [a,b,*]

[a] Department of Cardiology, Biomedical Engineering, Cardiovascular Institute, Thorax Center, Erasmus MC, Dr. Molewaterplein 40, Rotterdam, 3015GD, The Netherlands
[b] Department of Biomechanical Engineering, Delft University of Technology, Mekelweg 5, Delft, 2628 CD, The Netherlands
[c] Centre Ingénierie et Santé, Mines Saint-Étienne, 158 cours Fauriel, Saint-Etienne, 42023, France

ARTICLE INFO

Keywords:
Virtual fields method
Inverse problem
Heterogeneous material characterization
Atherosclerotic plaques
Hyperelasticity

ABSTRACT

Background and objective: Rupture of an atherosclerotic plaque in an artery is the primary cause of life-threatening cardiovascular events. Plaque rupture is closely associated with elevated mechanical stresses within the plaque. Stress analysis of plaques, which are structurally heterogeneous due to their multi-component composition, holds significant potential to improve the rupture risk assessment of plaques, guiding clinical decision making and surgical planning. A major challenge, however, lies in the efficient and accurate characterization of plaque-specific mechanical properties.

Methods: In this study, we introduce a novel framework based on the Virtual Fields Method (VFM) to identify the heterogeneous material properties of atherosclerotic plaques. We further propose a systematic strategy to generate virtual displacement fields (VDFs) tailored for pressurized tubular structures, such as the specific application of arteries, and determine the optimal number of VDFs for carotid artery plaques from ultrasound-derived measurements.

Results: The proposed framework achieved high accuracy in estimating the mechanical properties of individual plaque components, even when realistic levels of noise in the ultrasound data were considered. The computation time was 11 ± 2.5 s for pre-clinical ultrasound resolution and 8.6 ± 2.3 s for clinical ultrasound resolution.

Conclusion: This work presents the first implementation of VFM for the material characterization of heterogeneous atherosclerotic plaques. The robustness and computational efficiency of the framework provide a methodological basis for future studies toward in vivo plaque characterization.

1. Introduction

Many devastating cardiovascular events such as heart attack and ischemic stroke are caused by the rupture of an atherosclerotic lesion in an artery [1,2]. Atherosclerosis is a chronic, inflammatory disease of the arterial system, mainly affecting the conduit arteries such as coronaries and carotids [3]. The atherosclerotic lesion sites in the arteries, commonly referred to as plaques, are of heterogeneous structural composition, with the major macroscopic tissue components being diseased intima, lipid pools, and calcifications [4]. Plaque rupture brings the thrombogenic plaque content into contact with the blood, usually triggering thrombus formation in the bloodstream and occlusion in the arterial system [5]. To develop better treatment strategies, it is critical to assess the rupture risk of atherosclerotic plaques in the arteries of a patient. However, current clinical guidelines do not involve the plaque rupture risk assessment due to the lack of reliable and well-established methods to do so [6].

From an engineering viewpoint, plaque rupture is a tissue failure that is considered to occur when local mechanical stress exceeds the tissue strength. Finite element (FE) modeling can be used to calculate plaque stress distributions [4,7–9], thereby identifying mechanically vulnerable regions and supporting the assessment of plaque rupture risk. The reliability of these simulations are highly dependent on material behavior of the plaque components, especially of the diseased intima tissue, as the rupture occurs in this plaque component [8]. Various studies investigated the material behavior of atherosclerotic plaques experimentally, using mechanical tests such as uniaxial/biaxial tensile tests and unconfined compression tests [10–30]. Commonly

* Corresponding author.
E-mail address: a.akyildiz@tudelft.nl (A.C. Akyildiz).

https://doi.org/10.1016/j.cmpb.2026.109642
Received 1 September 2025; Received in revised form 31 August 2026; Accepted 7 September 2026
Available online 12 September 2026
0169-2607/© 2026 The Authors. Published by Elsevier B.V. This is an open access article under the CC BY license (http://creativecommons.org/licenses/by/4.0/).

plaques were regarded as homogeneous materials and the average, aggregate material properties were reported despite their heterogeneous, multicomponent structure. The reported plaque stiffness values spanned a wide range from 30 kPa to 270 MPa. This large variance in stiffness results was primarily attributed to compositional differences in plaques, as some plaques, for example, contain larger lipid pools, while some others contain smaller ones and are more of a calcified type [31]. Hence, for accurate stress analyses, material characterization of individual plaque components is of great importance.

In vivo measurements and ex vivo inflation tests of intact atherosclerotic arteries, combined with appropriate structural and deformation imaging techniques, have the potential to assess the material properties of individual plaque components. However, the material properties of the components can only be extracted using advanced analysis techniques from the acquired data. A commonly used method for this purpose is inverse FE modeling, also referred to as the FE modeling updating method [32–35]. The associated cost function is a measure of the difference between measured (or ground-truth) data and the FE simulation results obtained at each iteration. As a result, this approach is computationally expansive, as it requires a forward FE analysis at each iteration of a minimization procedure.

In contrast to inverse FE approaches, Virtual Fields Method (VFM) is based on defining and solving a set of equations derived from the principle of virtual work for a given boundary value problem [36]. VFM is an efficient approach, as this equation set can be solved analytically or through a numerical minimization procedure, without requiring heavy computations such as FE simulations at each iteration. Using full-field deformation measurements, VFM enables the identification of material parameters associated with an assumed constitutive relation. By defining virtual displacement fields (VDFs) that are appropriate for the examined boundary value problem, a set of equations is derived from the virtual work equation. Then, these equations are then either solved directly or employed within a minimization framework to identify the material constants in the constitutive relation. VFM has been used to characterize various engineering materials and, recently, also a few heterogeneously structured ones [37–40].

In this study, we have developed a framework to utilize VFM for the specific application of intraluminally pressurized, heterogeneous atherosclerotic arteries. The framework can also be utilized for the generic intraluminal pressurization of (multicomponent) tubular structures. Selecting suitable VDFs remains a challenge in VFM, as the choice of VDFs significantly affects the robustness and accuracy of material characterization [41]. For our application, we have proposed a novel strategy to identify optimal VDFs. We have validated our framework and assessed its performance using synthetic experimental data.

2. Method

2.1. Brief background on VFM

VFM is a method to identify the material constant values of an assumed constitutive relation for a continuum body from a measured full-field deformation data set. This section provides a brief description of the method. The reader is referred to other resources, such as [36], for a more in-depth explanation.

The method is based on the principle of virtual work. For a continuum body, where the position of its material points in the reference configuration is given by the position vector $\mathbf{X}$ and in the deformed/current configuration by the position vector $\mathbf{x}$, a function $\mathbf{x} = \phi(\mathbf{X})$ can be defined to map the position of each material point in the reference configuration to its position in the deformed configuration. In the case of a quasi-static equilibrium and absence of body forces, the principle of virtual work for a body can be prescribed in a three-dimensional Cartesian coordinate system of x, y, and z in the following form [36], where the internal virtual work is balanced by the external virtual work:

$$\underbrace{-\int_v \boldsymbol{\sigma} : \frac{\partial \mathbf{u}^*}{\partial \mathbf{x}} dv}_{IVW} + \underbrace{\int_S \mathbf{t} \cdot \mathbf{u}^* dS}_{EVW} = 0 \tag{1}$$

Here, v is the volume and S is the surface subjected to a force distribution of the continuum body in the current (deformed) configuration. $\boldsymbol{\sigma}$ is the Cauchy stress tensor and $\mathbf{t}$ is the traction vector for the surface forces applied on the body.

Eq. (1) is satisfied for any continuous function $\mathbf{u}^*$, referred to as a VDF, that is piecewise differentiable and kinematically admissible. Both the Cauchy stress tensor and the VDF are defined in the current configuration. The first term in the equation, the volume integral of the double dot product of the Cauchy stress tensor and the spatial gradient of the VDF, is referred to as the internal virtual work (work done by internal forces). The second term, the surface integral of the dot product of the virtual displacement field and the traction vector, is referred to as the external virtual work (work done by external forces). The Cauchy stress tensor is a function of the continuum body's material behavior and the real deformation the body underwent. If the applied traction and the full field deformation data are available, by defining appropriate and kinematically admissible VDF, the balance equation (1) can be reorganized to solve for the material constants of an assumed constitutive relation.

2.2. Developed VFM framework

2.2.1. Virtual work equation for pressurized tubular structures

The arteries in the human body are exposed to intraluminal blood pressure, which is the dominant force exerted on the arterial structure. Moreover, both healthy and diseased excised arteries are often tested in inflation test rigs to study their mechanical behavior [33–35,42,43] as this testing approach closely mimics the in vivo loading condition. In this study, this intraluminal pressurization of an atherosclerotic artery (both in vivo physiological pressurization and ex vivo inflation testing) is treated as a 2D, plane strain boundary value problem where the 2D plane contained the transversal cross-section of the artery [7]. On this artery cross-section, the only boundary condition is the traction due to the blood pressure exerted on the lumen surface of the atherosclerotic artery.

Atherosclerotic arteries are heterogeneous structures and are considered to consist of mechanically distinct (i.e., with different material behavior), homogenous components [4]. For the multicomponent structure, IVW in the balance equation (1) can be replaced by the sum of the internal virtual works of the individual tissue components (IVW_j's). Then, the balance equation (1) becomes

$$-\sum_{j=1}^{j_{max}} \left[\int_{v_j} \boldsymbol{\sigma} : \frac{\partial \mathbf{u}^*}{\partial \mathbf{x}} dv\right] + \int_S \mathbf{t} \cdot \mathbf{u}^* dS = 0 \tag{2}$$

where $j = 1, \ldots, j_{max}$ labels a structural component and v_j the component volume.

In this study, the structural components were modeled with incompressible Neo-Hookean hyperelastic material models. The Cauchy stress tensor for a Neo-Hookean material can be given as

$$\sigma = -p\mathbf{I} + 2\mu\mathbf{B} \tag{3}$$

where p is the hydrostatic pressure term, present due to the tissue incompressibility condition, $\mathbf{I}$ is the identity tensor and μ is the Neo-Hookean material constant (shear modulus), the value of which is to be determined with the VFM framework. $\mathbf{B}$ is the left Cauchy Green deformation tensor, defined as $\mathbf{B} = \mathbf{F}\mathbf{F}^T$ with $\mathbf{F}$ being the deformation gradient tensor in the Lagrangian description and defined as $\mathbf{F} = \frac{\partial \mathbf{x}}{\partial \mathbf{X}}$.

The deformation gradient tensor $\mathbf{F}$, and hence the left Cauchy Green deformation tensor $\mathbf{B}$ in Eq. (3) over the entire volume of the continuum

body under investigation are to be obtained from full-field deformation measurements. Some imaging modalities such as magnetic resonance imaging and ultrasound can provide full-field deformation measurements of atherosclerotic arteries in vivo and ex vivo. The acquired deformation measurements are usually outputted in a grid applied to the imaged structure, and the number and the size of the grid elements depend on the resolution of the imaging technique and postprocessing of the imaging data. VFM requires discretization of the volume and the loaded surface S accordingly. Hence, the surface integral EVW and the volume integrals IVW_j in Eq. (2) are to be approximated with discrete sums. Using discrete sums and replacing the Cauchy stress tensor term with Eq. (3), one can rewrite the balance equation (2) as

$$-\sum_{j=1}^{j_{max}}\left\{\sum_{k=1}^{k_{max}^{j}}[(-p_k\mathbf{I}+2\mu_j\mathbf{B}_k):\left.\frac{\partial\mathbf{u}^*}{\partial\mathbf{x}}\right|_k a_k t]\right\}+\sum_{s=1}^{s_{max}}[(\Delta P\ \mathbf{n}_s)\cdot\mathbf{u}^*(s)]l_s t=0 \tag{4}$$

Here, j labels again a tissue component and μ_j is the component's Neo-Hookean material constant. k labels the grid elements, with the total number of elements of k_{max}^{j} in the jth component and a_k is the surface area of the kth grid element. s labels the surface elements on the lumen and l_s is the length of the sth line element on S. t is the thickness and by dividing the whole equation by t, it is to be removed from the equation. The values of the components of $\mathbf{B}_k$, $\frac{\partial\mathbf{u}^*}{\partial\mathbf{x}}|_k$ and $\mathbf{u}^*(s)$ are evaluated at the center of the elements. It is worth noting that the traction vector $\mathbf{t}$ in EVW (see Eqs. (1) and (2)) is replaced by $\Delta P\mathbf{n}_s$ in Eq. (4), where ΔP is the pressure (orthogonal to the line elements) and $\mathbf{n}_s$ is the unit normal vector of the sth line element on S.

2.2.2. Optimization scheme

The left Cauchy Green deformation tensor $\mathbf{B}$ in Eq. (4) is to be obtained from measurements, which contain noise. Hence, rather than solving the set of equations derived from Eq. (4) analytically, the VFM framework was transformed into a minimization problem [44], where a cost function f was derived from Eq. (4) (after removing the thickness term) as

$$f=\sum_r\left\{-\sum_{j=1}^{j_{max}}\left\{\sum_{k=1}^{k_{max}^{j}}[(-p_k\mathbf{I}+2\mu_j\mathbf{B}_k):\left.\frac{\partial\mathbf{u}^{*r}}{\partial\mathbf{x}}\right|_k]\ a_k\right\}+\sum_{s=1}^{s_{max}}[\Delta P\ \mathbf{n}_s\cdot\mathbf{u}^{*r}(s)]\ l_s\right\}^2 \tag{5}$$

where r labels the VDFs. The value of the cost function f is driven by the choice of the unknown material constant values (μ_j-values) and defines the resulting quadratic difference between the internal virtual work and the external virtual work. The cost function f is minimized to yield the material constant values.

The minimization problem and the developed VFM framework were implemented in a custom-made MATLAB code. Trust Region Reflective (TRR) algorithm available in MATLAB (ver. R2024a) was utilized for the minimization problem. To reach the global minimum with the TRR algorithm, the MATLAB code was developed such that the minimization scheme ran 100 times, each one with a different set of initial guesses for μ_j-values of the tissue components, selected randomly from the parameter search range between 0 and 1 MPa. The median of the μ_j-values obtained from these 100 runs of the TRR algorithm is reported in this manuscript.

2.3. Generating virtual displacement fields

A critical step of VFM is to determine the VDFs for a specific problem. The boundary value problem associated with intraluminally pressurized atherosclerotic arteries involves heterogeneous configuration and hyperelastic material. While an optimized procedure for selecting VDFs has been developed for homogeneous configurations and linear elastic materials [45], such an approach is not applicable to this more complex scenario. Therefore, suitable VDFs specific to the intraluminal pressurization problem need to be formulated, followed by selecting optimal VDFs to accurately characterize each plaque component.

2.3.1. Strategy

It is important to note at this point that the hydrostatic pressure term p_k in the balance equation (4) can have a different value at each grid element in the structure. This dramatically increases the number of unknowns in the equation. By selecting VDFs with a trace of their spatial gradient equal to zero, i.e. $tr(\frac{\partial\mathbf{u}^*}{\partial\mathbf{x}})=0$, p_k can be removed. We identify a VDF with this feature and suitable for our plane strain, intraluminal pressurization boundary value problem as

$$\mathbf{u}^{*1}=\begin{bmatrix}\frac{x}{x^2+y^2}\\ \frac{y}{x^2+y^2}\\ 0\end{bmatrix} \tag{6}$$

Then the corresponding spatial gradient is

$$\frac{\partial\mathbf{u}^{*1}}{\partial\mathbf{x}}=\frac{1}{(x^2+y^2)^2}\begin{bmatrix}y^2-x^2 & -2xy & 0\\ -2xy & x^2-y^2 & 0\\ 0 & 0 & 0\end{bmatrix} \tag{7}$$

For convenience, the coordinate system is defined with it origin at the lumen center. The number of unknowns to be determined in Eq. (4), i.e., the Neo-Hookean material constants (μ_j) of the tissue components, depends on the number of the components. For instance, in the case of four components, four equations are derived from the balance equation (4), hence four VDFs, are required to have a system of mathematical equations that can be solved for the four unknown μ_j's. However, as mentioned above, the real-life full-field displacement data contains noise, hence we define a minimization problem with more than four VDFs.

We employ a fusion of two strategies to define new VDFs, derived from $\mathbf{u}^{*1}$. The first one is multiplying $\mathbf{u}^{*1}$ (Eq. (6)) with periodic functions. With this approach, a set of new VDFs can be obtained as

$$\mathbf{u}^{*2n}=\mathbf{u}^{*1}cos^{2n}(\theta),\qquad\text{with}\qquad n=1,2,3...,n_{max} \tag{8}$$

and

$$\mathbf{u}^{*2n+1}=\mathbf{u}^{*1}sin^{2n}(\theta),\qquad\text{with}\qquad n=1,2,3...,n_{max} \tag{9}$$

where θ defines the angle between the x-axis and the line segment from the coordinate system origin to the center of grid element, given by

$$\theta=cos^{-1}(\frac{x}{\sqrt{x^2+y^2}})=sin^{-1}(\frac{y}{\sqrt{x^2+y^2}}) \tag{10}$$

The second strategy to define new VDFs is rotating the atherosclerotic artery cross-section by an angle of θ_i defined as

$$\theta_i=i\frac{\pi}{m},\qquad\text{with}\qquad i=0,1,2,\dots,m-1 \tag{11}$$

Then, the descriptions of the ultimate VDFs become

$$\mathbf{u}^{*2m(n-1)+2(i+1)}=\mathbf{u}^{*1}cos^{2n}(\theta+\theta_i),\qquad\text{with}\qquad n=1,2,3...,n_{max}\quad i=0,1,2,\dots,m-1 \tag{12}$$

and

$$\mathbf{u}^{*2m(n-1)+2(i+1)+1}=\mathbf{u}^{*1}sin^{2n}(\theta+\theta_i),\qquad\text{with}\qquad n=1,2,3...,n_{max}\quad i=0,1,2,\dots,m-1 \tag{13}$$

Here m and n_{max} are integer numbers of preference. Eqs. (6), (12), and (13) define the complete set of VDFs for the 2D, plane strain, intraluminal pressurization boundary value problem of an atherosclerotic artery. An example case is presented in Appendix A.

2.3.2. Optimal number of VDFs

A finite number of VDFs can be generated by selecting the values of n_{max} and m in Eqs. (12) and (13). To identify the optimal values of n_{max} and m, a grid search procedure was employed. The identification procedure was performed for various combinations, and the optimal parameter combination was selected based on the relative error (RE) in the estimated results. The RE of a component was defined as

$$RE = |\frac{\mu_{VFM} - \mu_{GT}}{\mu_{GT}}| \quad (14)$$

where μ_{VFM} is the predicted value with the developed VFM framework and μ_{GT} is the ground truth value.

Relative error maps were created with combinations of different n_{max} and m values using a test dataset, created synthetically (see Section 2.4). For each plaque component, parameter regions producing a relative error below a specified threshold were identified. Subsequently, an overlapping region among the key components was determined, and the parameter combination located at the center of this overlapping region was selected as optimal. This procedure was repeated across the entire test dataset, and the median optimal parameter combination was chosen to generate the final optimal VDF.

Rupture of the diseased intima component, and specifically of the fibrous cap overlying a lipid pool, is the main cause of cardiovascular events [46]. It is therefore considered to be more important to estimate the diseased intima material properties more accurately than the other components. Hence, the regions producing low relative error values for the diseased intima and the arterial wall were first identified. The overlap between these combinations and those also yielding low error values for calcified tissue and lipid was then determined. The final optimal number of VDFs was selected from the overlapping region identified through this refined selection approach.

2.4. Synthetic experimental data for optimizing the total number of VDFs

Synthetic experimental full-field displacement data was generated by FE simulations of ten atherosclerotic carotid arteries to determine the optimal number of VDFs.

2.4.1. Finite element models

2D FE plaque geometries were obtained from the structural segmentation of histology images of 10 human atherosclerotic carotid plaques (Appendix B), acquired from carotid endarterectomy surgery, where the plaques had been separated from the healthy arterial wall. An example is shown in Fig. 1. The sections were histochemically stained with standard Hematoxylin & Eosin staining, which allowed obtaining the geometries of the plaque components, i.e., diseased intima, lipid pool, and calcifications. Please refer to [47] for a detailed description. The fourth component of an atherosclerotic artery, the healthy wall, was created by adding a uniform layer of 1 mm thickness [48]. Eventually, the FE atherosclerotic artery models included four components: diseased intima, lipid, calcified tissue, and healthy arterial wall (Fig. 1b).

Incompressible Neo-Hookean material models were used for all four tissue components. The values of the material constant μ (Eq. (3)) assigned to each component are as follows: diseased intima (DI): 120 kPa, lipid (L): 5 kPa, calcified tissue (CT): 423 kPa, and wall (W): 250 kPa [15,49]. The geometries were meshed with plane strain quadrilateral elements with an average edge length of 50 μm, which resulted in 17 thousands elements on average for each FE model. An intraluminal blood pressure of 100 mmHg (13.33 kPa) was applied as the loading condition, to mimic the mean blood pressure. The rigid body motion was constrained by fixing a single node on the outer edge both for x and y displacement. FE simulations were performed with ABAQUS/Standard (ver. 2016, Dassault Systems).

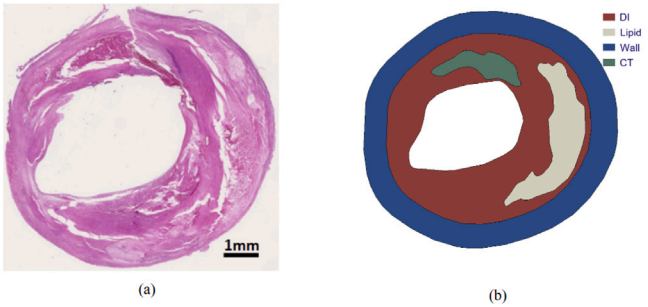

Fig. 1. Segmented plaque geometry based on histological analysis of an atherosclerotic human carotid artery: (a) Histology image, and (b) Segmented geometry. [Red = Diseased Intima (DI), Beige = Lipid, Green = Calcified Tissue (CT), Blue = Healthy Wall Tissue (Wall)]

2.4.2. Synthetic deformation measurements

For full-field displacement measurements of atherosclerotic arteries, ultrasound imaging is a suitable technique [50,51]. This technique has been used both for in vivo physiological deformation measurements [52] and ex vivo inflation testing measurements [33]. For the former, clinical ultrasound scanners are used, operating at center frequencies of 5–10 MHz, commonly with a linear-array transducer and a frame rate of 100 Hz [33]. For the latter, preclinical ultrasound scanners with higher spatial resolution are employed, operating at center frequencies of 20–55 MHz with a linear-array transducer [53]. For the former, clinical ultrasound scanners and for the latter, higher spatial resolution, preclinical ultrasound scanners are used. We created synthetic experimental displacement data, to be used for the developed VFM framework as input, from the nodal displacement data obtained with the FE simulations, to analyze both the clinical and pre-clinical ultrasound imaging scenarios. Therefore, FE displacement results were resampled at 75 μm × 275 μm resolution (clinical scanner resolution, in vivo deformation case, axial × lateral) and at 15 μm × 55 μm resolution (preclinical scanner resolution, ex vivo inflation testing case, axial × lateral). The resulting synthetic displacement data were then used as input full-field displacement data for the developed VFM framework.

Random Gaussian noise was added to the synthetic displacement data to simulate uncertainty representative of ultrasound-based displacement measurement. The noise level applied was twice the magnitude of previously reported values for ultrasound-based displacement measurements [52]. For the clinical ultrasound scanner case, noise levels of 3% and 9% of the measured displacement were applied in the axial and lateral directions of the ultrasound beam, respectively. For the non-clinical, high-frequency ultrasound scanner case, the noise levels were scaled linearly with the scanner's spatial resolution, resulting in axial and lateral noise levels of 0.6% and 1.8%, respectively.

2.5. Overview of the framework

A graphical overview of the developed VFM framework is shown in Fig. 2, which consists of two main stages: selection of optimal VDFs and application of the framework for material parameter identification. In the first stage, the optimal VDFs are selected using segmented histology, synthetic FE-generated displacement fields, and prescribed lumen pressure. In the present study, the VDF selection is performed using a representative atherosclerotic carotid geometry set (n = 10) for pre-clinical and clinical ultrasound settings, and the resulting optimal parameters (m and n_{max}) are directly applicable to future ultrasound-based applications under comparable imaging conditions. In the second stage, the developed framework is applied to identify material properties. The required inputs are: (i) a segmented atherosclerotic artery geometry obtained from a structural imaging modality, (ii) full-field

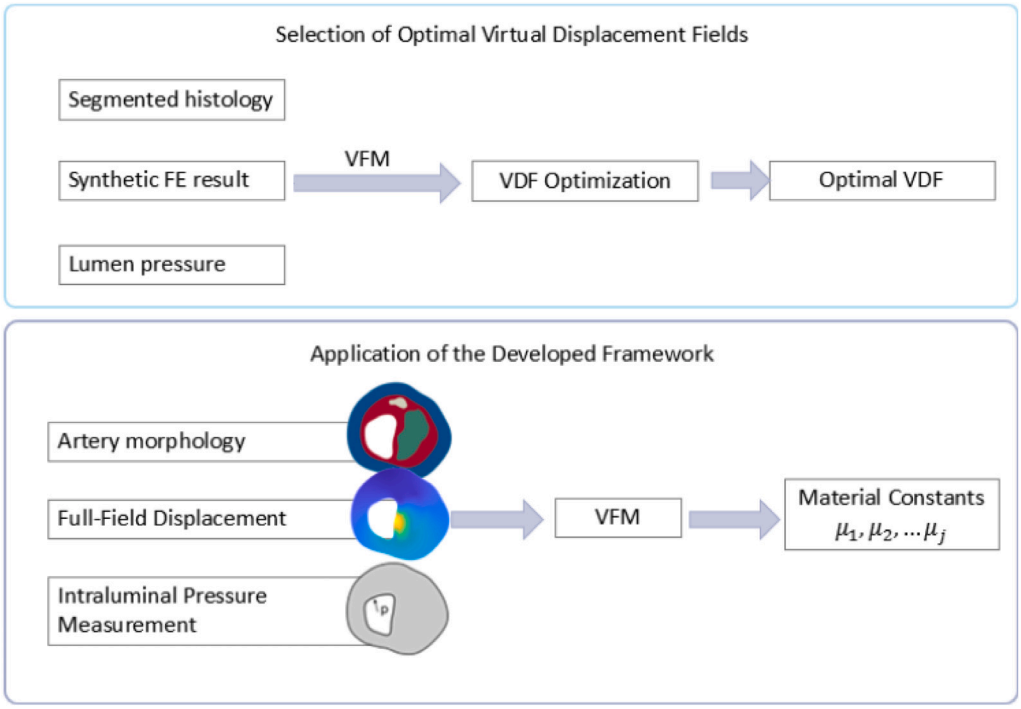

Fig. 2. Schematic overview of the developed VFM framework for atherosclerotic plaque material characterization. The framework consists of two stages. Stage 1 is the selection of optimal VDFs, while Stage 2 performs the material parameter identification. For the ultrasound imaging conditions considered in this study, only Stage 2 is required for practical application.

intraplaque displacement data, and (iii) intraluminal pressure measurements. Notably, for the ultrasound systems for which this framework was developed, the second stage is the only step required for practical application.

2.6. Performance assessment of the developed VFM framework

The performance of the developed VFM framework was evaluated, using a set of 10 human carotid arteries (Appendix C) different than the ones used for the test data set to assess the framework's capability to handle geometric complexity. The optimal VDF parameters were first identified using a set of 10 plaque geometries containing one lipid and one calcified tissue component (Appendix B). These parameters were then fixed and Stage 2 of the framework was subsequently applied to a separate dataset (Appendix C) of 10 more complex plaque geometries with multiple lipid pools, calcifications, and more intricate component boundaries for material parameter identification. Although the performance assessment focuses on Stage 2, synthetic FE-generated displacement data, generated using the same procedure described in Section 2.4, were used to enable direct comparison with known ground-truth material parameters. The material constants of the atherosclerotic artery components for the 10 carotid arteries were predicted with the developed VFM framework, using the data with and without noise, and compared to the ground truth values.

3. Results

3.1. Representative case

A representative artery (#1) for the pre-clinical scanner case is illustrated in Fig. 3, demonstrating the steps to estimate the Neo-Hookean material constant (μ) values using the proposed VFM method. The atherosclerotic plaque contained one calcified tissue and one lipid, as illustrated in Fig. 3a and b. An FE model was constructed accordingly, featuring a large lipid region with an area ratio of 30% and a calcified tissue occupying 2% of total plaque area, indicating an advanced stage of atherosclerotic plaque.

FE analysis-derived displacement under intraluminal pressure is given in Fig. 3c, with the highest displacement occurring near the lumen where the lipid component is located, as the compliant nature of the lipid leads to larger deformations. Conversely, in the calcified tissue the displacement was nearly zero due to the high stiffness, which resists deformation. The FE displacement results were down-sampled to mimic the displacement measurement resolutions obtained from ultrasound. The distribution and range of the displacement field remained similar after this process.

As shown in Fig. 3d, the relative error plots show the combinations resulting in an error of less than 10%. For the diseased intima and arterial wall, all combinations within the search range produced an error of less than 10%. The lipid component exhibited lower error values in the range of 4 to 9 periodic functions and was less sensitive to variations in rotations. The calcified tissue exhibited larger errors, compared to the other three tissue components, possibly due to its small area ratio (2% of the plaque area).

For this representative case, the optimal combination was achieved when $n_{max} = 4$ and $m = 13$, resulting in 105 VDFs in the objective function.

3.2. Optimal number of virtual displacement fields

The developed VFM-based framework was applied to the first set of ten atherosclerotic arteries using two resolution settings to find the optimal VDFs. Each artery contained one lipid pool and one calcified tissue. The optimal VDFs were obtained based on μ-values of the diseased intima, as described in Section 2.6.

For the preclinic scanner case, the trend observed across all ten arteries was similar to the representative case. The size of this optimal region is component-dependent: a wide range of combinations resulted in μ-values with less than 10% error for diseased intima and arterial wall, while the range was narrower for lipid and calcified tissue.

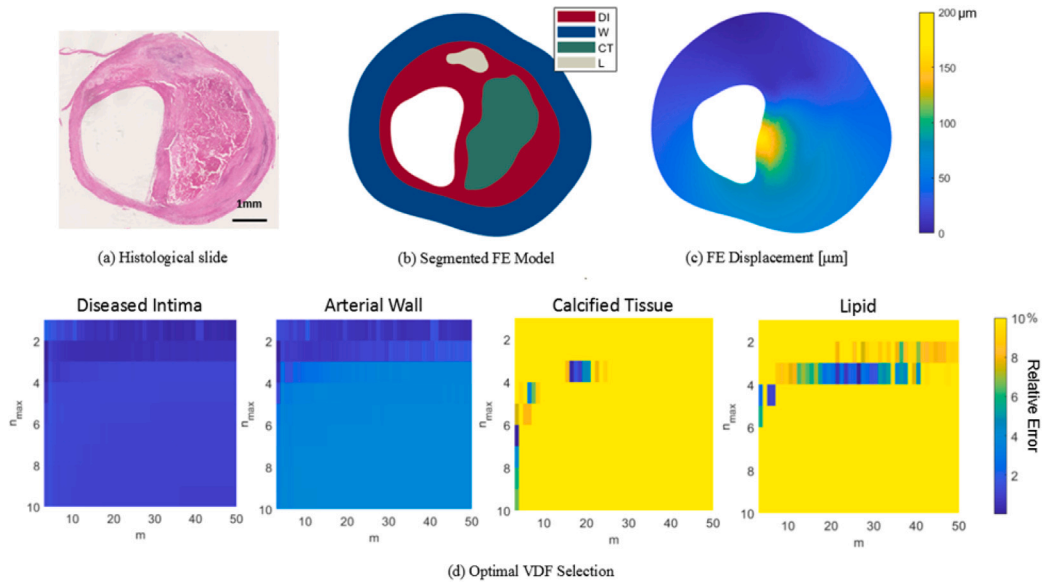

Fig. 3. Demonstration of the developed VFM-based method with the use of the representative artery #1: (a) histology, (b) segmented FE model, (c) displacement from FEM [μm], (d) relative error maps [%] of estimated material parameters for the four tissue components, shown for different combinations of the maximum number of periodic functions n_{max} and the number of rotations m.

Table 1
Optimal number of n_{max} and m.

	Artery	1	2	3	4	5	6	7	8	9	10	Median
Pre-clinic Scanner	n_{max}	4	6	3	7	6	7	6	8	3	3	6
	m	13	27	10	28	19	28	27	35	17	34	27
Clinical Scanner	n_{max}	1	6	2	5	2	3	4	8	3	6	4
	m	27	27	17	2	10	18	14	2	12	27	14

Table 1 presents the optimal combinations for all cases for the pre-clinic scanner. The range of n_{max} was from 3 to 8, and for the rotations, it was from 10 to 34. The median values of all ten arteries were $n_{max} = 6$ and $m = 27$, which were used as the optimal combination in the subsequent analyses for the pre-clinic scanner.

For the clinical ultrasound scanner case, fewer combinations could achieve an error of less than the set threshold. Although the range of the combinations was smaller, the overall trend was similar to that of the high-frequency scanner. For the clinical scanner resolution, n_{max} ranged from 1 to 8, and the number of rotations ranged from 2 to 27, achieving an error below 20% (Table 1). The medians of optimal numbers for all ten arteries were $n_{max} = 4$ and $m = 14$.

3.3. Performance of the VFM framework

Every artery in the second set of carotids (n = 10) contained a lipid pool and calcified tissue. The estimated μ-values of all four components at two resolution settings were obtained using the optimal VDFs found in the previous section (for pre-clinic scanner case: $n_{max} = 6$ and $m = 27$, and for clinical case: $n_{max} = 4$ and $m = 14$). The proposed method, coded in MATLAB, required 11 ± 2.5 s for the pre-clinic scanner and 8.6 ± 2.3 s for the clinical scanner resolution. All analyses were performed on a workstation with an Intel(R) Xeon(R) Gold 6248R processor at 3 GHz with 32 GB of RAM.

No noise case: The predicted μ-values for the no-noise case are given in Table 2. For the pre-clinic scanner case, the predictions demonstrated high accuracy and limited variance. The median (25th–75th percentile, $Q_1 - Q_3$) μ-values were 118.4 (114.8–121.2) kPa for diseased intima, 258.8 (248.7–264.3) kPa for the arterial wall, 4.4 (3.5–6.3) kPa for the lipid pool, and 399.8 (348.3–434.9) kPa for calcified tissue, closely aligning with the ground-truth values. For the clinical scanner case, the predicted μ-values exhibited lower accuracy and a larger variance compared to the pre-clinic scanner case. The median (25th–75th percentile, $Q_1 - Q_3$) μ-values were 127.3 (125.4–130.6) kPa for diseased intima, 225.5 (203.8–251.1) kPa for the arterial wall, 5.0 (1.2–7.5) kPa for the lipid pool, and 415.3 (360.1–610.1) kPa for calcified tissue.

Noisy data case: The predicted μ-values for the noisy data case are given in Table 3. For the pre-clinic scanner, the predicted μ-values were minimally affected by the noise. The median (IQR) values were 118.4 (114.2–120.3) kPa for diseased intima, 258.8 (245.8–290.9) kPa for the arterial wall, 4.8 (2.9–8.6) kPa for the lipid pool, and 412.0 (303.1–455.0) kPa for calcified tissue. For the clinical scanner case, the predicted μ-values were 125.3 (117.9–126.5) kPa for diseased intima, 247.8 (214.6–289.0) kPa for the arterial wall, 1.3 (0.59–2.5) kPa for the lipid pool, and 433.5 (291.4–534.4) kPa for calcified tissue. Overall, while the measurement noise introduced a larger variance, the performance of the framework remained consistent with that observed in the no-noise cases.

4. Discussion

Plaque stress analyses may play a critical role in cardiovascular risk management in the future [8]. Reliable stress results require correct information on plaque material properties. This paper presented a novel VFM framework for estimating the component-wise material properties of heterogenous atherosclerotic arteries using in vivo deformation or ex vivo inflation data. To the best of our knowledge, the current study is the first that applies VFM to extract the mechanical properties of atherosclerotic arteries. Previous studies presented ways to do so mainly employing iFEM [33–35,49,54,55]. However, the major drawback of iFEM is the high simulation time required. As demonstrated in a prior study, identifying multicomponent atherosclerotic plaque properties via iFEM can require approximately 7 h [35]. Our VFM-based

Table 2
Estimated μ-values [kPa] without noise. Values are reported as median (IQR).

	Pre-clinic scanner				Clinic scanner			
	DI	W	L	CT	DI	W	L	CT
GT	120	250	5	423	120	250	5	423
Case 1	129.6 (2.9)	241.4 (9.0)	6.3 (2.5)	418.8 (3.4)	129.9 (0.9)	167.4 (3.2)	25.9 (1.1)	523.9 (1.9)
Case 2	109.8 (0.6)	300.0 (0.9)	4.0 (2.2)	377.1 (0.2)	152.1 (0.6)	120.6 (3.7)	53.0 (2.0)	638.9 (6.0)
Case 3	113.6 (1.6)	263.3 (2.3)	4.9 (1.4)	410.3 (2.4)	110.6 (1.9)	282.6 (2.4)	7.5 (2.0)	376.3 (2.5)
Case 4	114.6 (0.2)	248.4 (0.4)	8.3 (0.7)	304.5 (8.7)	126.0 (0.3)	214.9 (0.4)	7.5 (0.8)	246.8 (9.3)
Case 5	120.3 (0.3)	257.6 (0.7)	3.7 (0.1)	440.3 (26.0)	126.0 (0.3)	248.6 (1.0)	1.1 (0.2)	430.1 (37.7)
Case 6	118.8 (2.5)	264.6 (3.0)	6.3 (1.7)	450.7 (107.5)	133.0 (0.4)	202.3 (2.6)	1.3 (1.7)	1033.0 (54.0)
Case 7	105.3 (2.7)	259.5 (3.5)	3.7 (1.8)	2547.5 (114.1)	104.6 (3.9)	260.5 (5.4)	4.2 (3.1)	2550.8 (18.3)
Case 8	130.8 (1.6)	252.0 (5.3)	6.3 (2.3)	400.6 (13.5)	130.8 (1.9)	251.7 (6.6)	6.2 (2.7)	401.1 (16.3)
Case 9	121.5 (0.1)	249.4 (0.2)	1.7 (0.9)	338.7 (21.6)	125.8 (0.0)	236.0 (0.1)	0.7 (0.7)	354.8 (13.3)
Case 10	118.6 (0.0)	244.4 (0.2)	2.2 (0.9)	278.6 (6.8)	128.7 (0.0)	208.2 (0.2)	0.4 (0.9)	202.3 (6.7)
Median (Q_1–Q_3)	118.4 (114.8–121.2)	258.8 (248.7–264.3)	4.4 (3.5–6.3)	399.8 (348.3–434.9)	127.3 (125.4–130.6)	225.5 (203.8–251.1)	5.0 (1.2–7.5)	415.3 (360.1–610.1)

Table 3
Estimated μ-values [kPa] with noise. Values are reported as median (IQR).

	Pre-clinic scanner				Clinic scanner			
	DI	W	L	CT	DI	W	L	CT
GT	120	250	5	423	120	250	5	423
Case 1	120.0 (1.0)	206.9 (0.7)	42.0 (0.4)	457.5 (0.3)	122.5 (1.2)	214.2 (4.5)	10.1 (1.1)	475.5 (1.1)
Case 2	110.0 (0.7)	299.7 (0.9)	3.3 (2.2)	377.1 (0.1)	130.6 (0.2)	298.3 (1.9)	2.5 (2.2)	307.3 (4.0)
Case 3	108.7 (1.2)	376.1 (1.7)	1.6 (0.9)	225.2 (1.6)	102.2 (0.1)	408.1 (0.1)	0.2 (0.2)	119.4 (0.0)
Case 4	113.0 (0.2)	254.5 (0.3)	8.9 (0.5)	271.7 (6.8)	119.6 (0.1)	239.9 (0.1)	1.6 (0.5)	286.1 (3.3)
Case 5	117.9 (0.3)	263.0 (0.8)	3.5 (0.1)	638.3 (29.4)	126.8 (0.3)	255.7 (0.5)	0.9 (0.2)	637.9 (18.6)
Case 6	140.1 (0.7)	175.9 (0.2)	9.6 (1.4)	4379.1 (175.2)	161.3 (0.0)	129.4 (0.0)	0.1 (0.2)	549.4 (3.3)
Case 7	118.4 (3.7)	264.5 (4.4)	6.2 (2.5)	446.8 (161.7)	117.2 (0.4)	261.1 (0.7)	0.7 (0.4)	1085.6 (3.4)
Case 8	131.2 (2.0)	354.5 (8.1)	7.6 (2.6)	319.1 (17.1)	117.4 (0.6)	315.0 (2.5)	2.4 (0.9)	391.4 (4.3)
Case 9	118.5 (0.1)	253.0 (0.2)	2.7 (1.1)	447.6 (24.1)	124.5 (0.0)	215.9 (0.0)	0.6 (0.9)	489.6 (2.5)
Case 10	120.4 (0.0)	243.4 (0.2)	2.8 (0.9)	297.8 (6.6)	125.5 (0.0)	204.8 (0.0)	13.5 (0.5)	194.3 (0.8)
Median (Q_1–Q_3)	118.4 (114.2–120.3)	258.8 (245.8–290.9)	4.8 (2.9–8.6)	412.0 (303.1–455.0)	125.3 (117.9–126.5)	247.8 (214.6–289.0)	1.3 (0.6–2.5)	433.5 (291.4–534.2)

framework addresses this challenge and dramatically reduces the computational time to seconds, making our method more resource-efficient and suitable for future clinical applications.

The proposed framework provided accurate estimations of the material properties of the atherosclerotic artery tissue components. In particular, the diseased intima, the key component associated with plaque rupture [8], was estimated with high accuracy in both imaging scenarios. This accuracy was maintained in the presence of measurement noise, demonstrating the robustness of the framework under noisy conditions. In addition, the framework effectively handles geometric and morphologic complexity, as its performance was evaluated on plaque geometries more complex than those used during framework development, including cases with multiple lipid pools, calcifications, and irregular component boundaries.

A relatively lower accuracy was achieved for calcified tissue and lipid pool. This may be partly attributed to the smaller size of these components. The area of a component is positively related to its contribution to the cost function minimized (Eq. (5)), and therefore, the value of the cost function is less sensitive to the change in the μ-values of these components. This effect is amplified when the component is far from the lumen, as the VDF values are inversely correlated with the radial distance from the lumen center (Eq. (6)). It is worth to note that stiffness of small calcified tissue and lipids has a limited impact on plaque risk assessment. Future studies could focus on enhancing small component stiffness accuracy by redesigning the VDFs and/or the cost function and investigating geometry-dependency of the developed framework.

A critical aspect of VFM is the appropriate selection of VDFs, as this significantly affects the robustness and accuracy of the material characterization process [41]. In this study, we address this by proposing a novel approach to generating VDFs was introduced in our study by multiplying a base VDF with periodic functions and applying rotations. The major advantage of this approach is its ability to generate theoretically infinitely many VDFs, allowing for the formulation of an overdetermined identification system, with more VDFs than unknown parameters, thereby reducing sensitivity to experimental noise. The robustness of the proposed framework to measurement noise is demonstrated in our performance assessment, where material property estimates are obtained in a fairly stable fashion in the presence of input data noise. While developed for the estimation of plaque material properties under intraluminal pressurization, this method shows potential for broader application. The constructed VDFs may be applicable to other tubular structures subjected to similar loading. Moreover, we introduce a strategy to select the optimal VDFs for complex multi-component structures. This task is particularly challenging in such cases, as each constituent may respond differently to loading, requiring distinct VDF to extract reliable local information. This strategy can be extended beyond arterial plaques to other heterogeneous materials. These aspects highlight the potential value of the method for a wider range of VFM-based biomechanical and material characterization problems.

There are some limitations associated with the framework developed. First, the method was tested using a Neo-Hookean model, which is a relatively simple isotropic hyperelastic material model. It was selected to assess the framework's capability to identify multiple material parameters in a heterogeneous plaque configuration. Although it may not fully capture the mechanical behavior of the diseased intima, the Neo-Hookean model remains widely used in the literature [56,57]. Moreover, the proposed VFM framework is not restricted to Neo-Hookean model and can be extended to more complex constitutive

models. The use of multiple VDFs enables the generation of various systems of independent equations, which is necessary to reliably identify the increased number of material parameters. Future work may focus on extending the framework to capture more complex material behavior, such as locally heterogeneous and anisotropic ones.

Another limitation is that, as it is in current state, the framework requires a priori knowledge of the component boundaries. Segmentation inaccuracies of certain components may affect the accuracy of the identified material property, with the other plaque constituents remain largely unaffected. However, in the present study, minor boundary perturbations were inherently introduced when resampling the fine-scale FE displacement fields onto the coarser grid used as an input for the VFM framework. Yet, the material parameter estimations were fairly accurate, indicating robustness to moderate segmentation inaccuracies.

The framework was developed and validated for the 2D plane-strain problem, assuming that deformation occurs predominantly within the cross-sectional plane with negligible or zero out-of-plane strain. This assumption is supported by previous studies reporting that axial strain is substantially smaller than in-plane strain for arteries under physiological loading [58,59]. However, in regions with complex plaque geometries or near arterial bifurcations, out-of-plane deformation may become non-negligible due to stronger local three-dimensional effects. In such cases, a 3D formulation would be more appropriate.

The proposed framework does not account for residual stresses or in vivo pre-stresses. Previous studies have shown that residual stresses can substantially redistribute arterial wall stresses and alter local stress within the fibrous cap [60]. For the present application using a Neo-Hookean constitutive model, the limited nonlinearity of the stress–strain response reduces sensitivity to pre-stress effects. However, extending the framework to more strongly nonlinear constitutive models will require explicit considerations and modifications in the framework. Computational approaches based on inverse finite element methods and iterative geometry-updating algorithms have been proposed to estimate unloaded geometries or the associated residual stress field [61,62]. The estimated zero-stress configuration can be subsequently be combined with measured deformation fields and incorporated into the proposed framework as the reference state for material identification.

5. Conclusion

A VFM-based framework is developed for characterizing the material properties of heterogeneous atherosclerotic plaques. The framework addresses the challenges associated with applying the virtual fields method to heterogeneous structures. It was evaluated under two full-field displacement measurement scenarios commonly used for carotid artery assessment. The results showed close agreement between the identified parameters and the ground-truth values, particularly for the diseased intima. The proposed framework provides a computationally efficient approach for characterizing atherosclerotic plaques and represents a step toward in vivo mechanical characterization of arterial tissues.

CRediT authorship contribution statement

Yanjing Liu: Writing – original draft, Validation, Software, Methodology. **Ronald D. van den Berg:** Methodology, Conceptualization. **Frank J.H. Gijsen:** Writing – review & editing, Supervision. **Stéphane Avril:** Writing – review & editing, Conceptualization. **Ali C. Akyildiz:** Writing – review & editing, Supervision, Funding acquisition.

Ethics in publishing statement

All authors agree that:

This research presents an accurate account of the work performed, all data presented are accurate and methodologies detailed enough to permit others to replicate the work.

This manuscript represents entirely original works and or if work and/or words of others have been used, that this has been appropriately cited or quoted and permission has been obtained where necessary.

This material has not been published in whole or in part elsewhere.

The manuscript is not currently being considered for publication in another journal.

During the preparation of this work, the authors used ChatGPT to check grammar and improve readability. After using this tool, the authors reviewed and edited the content as needed and take full responsibility for the content of the publication.

That generative AI and AI-assisted technologies have not been used to create or alter images unless specifically used as part of the research design where such use must be described in a reproducible manner in the methods section.

All authors have been personally and actively involved in substantive work leading to the manuscript and will hold themselves jointly and individually responsible for its content.

Declaration of competing interest

The authors declare the following financial interests/personal relationships which may be considered as potential competing interests: Ali C. Akyildiz reports financial support was provided by European Research Council. If there are other authors, they declare that they have no known competing financial interests or personal relationships that could have appeared to influence the work reported in this paper.

Acknowledgments

This work was supported by the European Research Council (ERC, Grant No. 101042724).

Appendix A. Generation of virtual displacement fields - examples

Virtual displacement fields are generated based on Eqs. (6), (12), and (13). For a given number of periodic functions n_{max} and rotation m, the total number of VDFs generated is $2n_{max} \cdot m + 1$. An example case is given here when $n_{max} = 2$ and $m = 2$.

This results in $n_{max} = 2$ and $i = [0, 1]$, hence $\theta_i = [0, \frac{\pi}{2}]$ and four periodic functions of cos^2, sin^2, cos^4 and sin^4. A set of 9 virtual fields is generated as follows:

Indices	Expression
$n = 1, i = 0$	$\mathbf{u}^{*2} = \mathbf{u}^{*1} \cos^2(\theta)$
	$\mathbf{u}^{*3} = \mathbf{u}^{*1} \sin^2(\theta)$
$n = 1, i = 1$	$\mathbf{u}^{*4} = \mathbf{u}^{*1} \cos^2\left(\theta + \frac{\pi}{2}\right)$
	$\mathbf{u}^{*7} = \mathbf{u}^{*5} \sin^2\left(\theta + \frac{\pi}{2}\right)$
$n = 2, i = 0$	$\mathbf{u}^{*6} = \mathbf{u}^{*1} \cos^4(\theta)$
	$\mathbf{u}^{*5} = \mathbf{u}^{*7} \sin^4(\theta)$
$n = 2, i = 1$	$\mathbf{u}^{*8} = \mathbf{u}^{*1} \cos^4\left(\theta + \frac{\pi}{2}\right)$
	$\mathbf{u}^{*9} = \mathbf{u}^{*1} \sin^4\left(\theta + \frac{\pi}{2}\right)$

Appendix B. Carotid artery models for obtaining optimal combination of virtual fields

See Fig. B.4.

Appendix C. Carotid artery models for performance analysis

See Fig. C.5.

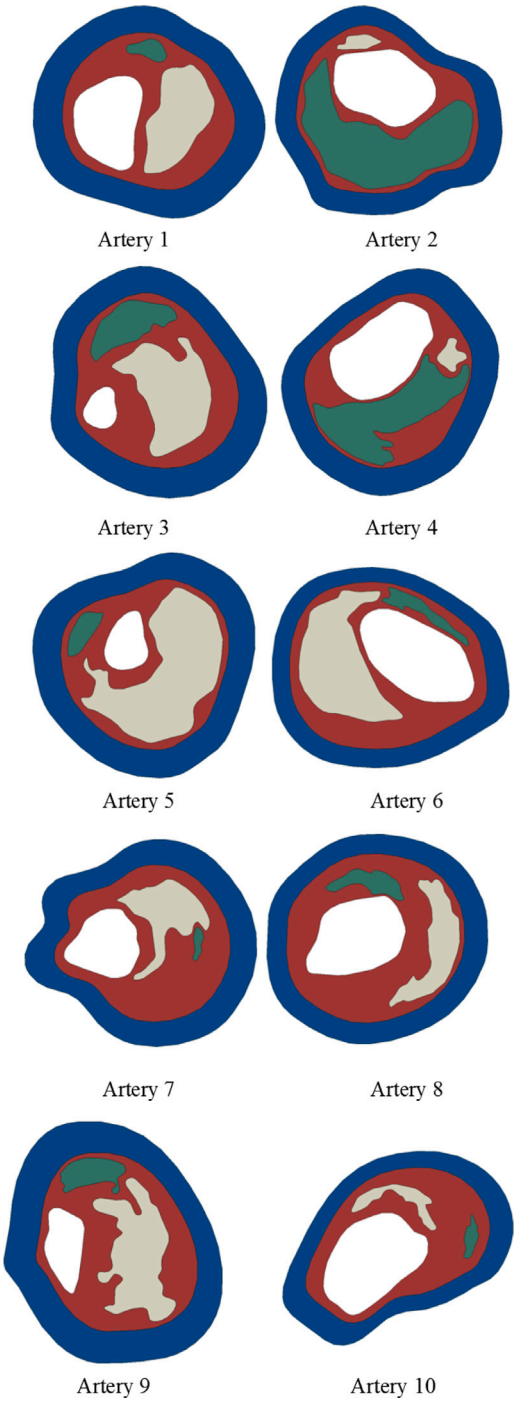

Fig. B.4. Segmentations of the arteries based on the histological slides, Red = Diseased intima (DI), White = Lipid, Green = Calcified Tissue (CT), Blue = Healthy Wall Tissue.

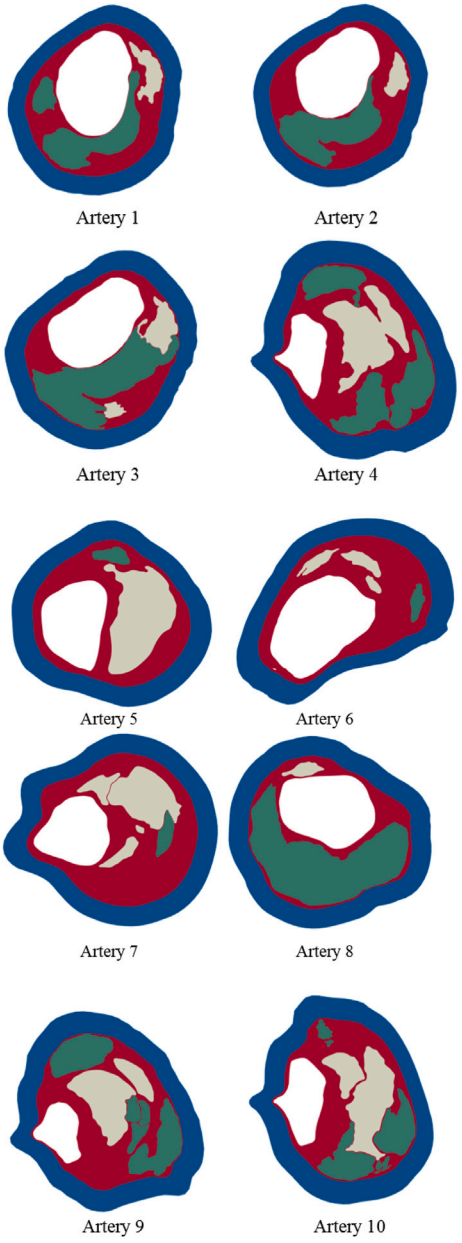

Fig. C.5. Segmentations based on the histological slides, Red = Diseased intima (DI), White = Lipid, Green = Calcified Tissue (CT), Blue = Healthy Wall Tissue.

Data availability

The code and datasets are available upon reasonable request.

References

[1] R. Lozano, M. Naghavi, K. Foreman, S. Lim, K. Shibuya, V. Aboyans, J. Abraham, T. Adair, R. Aggarwal, S.Y. Ahn, M. Alvarado, H.R. Anderson, L.M. Anderson, K.G. Andrews, C. Atkinson, L.M. Baddour, S. Barker-Collo, D.H. Bartels, M.L. Bell, E.J. Benjamin, D. Bennett, K. Bhalla, B. Bikbov, A. Bin Abdulhak, G. Birbeck, F. Blyth, I. Bolliger, S. Boufous, C. Bucello, M. Burch, P. Burney, J. Carapetis, H. Chen, D. Chou, S.S. Chugh, L.E. Coffeng, S.D. Colan, S. Colquhoun, K.E. Colson, J. Condon, M.D. Connor, L.T. Cooper, M. Corriere, M. Cortinovis, K.C. de Vaccaro, W. Couser, B.C. Cowie, M.H. Criqui, M. Cross, K.C. Dabhadkar, N. Dahodwala, D. De Leo, L. Degenhardt, A. Delossantos, J. Denenberg, D.C. Des Jarlais, S.D. Dharmaratne, E.R. Dorsey, T. Driscoll, H. Duber, B. Ebel, P.J. Erwin, P. Espindola, M. Ezzati, V. Feigin, A.D. Flaxman, M.H. Forouzanfar, F.G. Fowkes, R. Franklin, M. Fransen, M.K. Freeman, S.E. Gabriel, E. Gakidou, F. Gaspari, R.F. Gillum, D. Gonzalez-Medina, Y.A. Halasa, D. Haring, J.E. Harrison, R. Havmoeller, R.J. Hay, B. Hoen, P.J. Hotez, D. Hoy, K.H. Jacobsen, S.L. James, R. Jasrasaria, S. Jayaraman, N. Johns, G. Karthikeyan, N. Kassebaum, A. Keren, J.P. Khoo, L.M. Knowlton, O. Kobusingye, A. Koranteng, R. Krishnamurthi, M. Lipnick, S.E. Lipshultz, S.L. Ohno, et al., Global and regional mortality from 235 causes of death for 20 age groups in 1990 and 2010: a systematic analysis for the global burden of disease study 2010, Lancet 380 (9859) (2012) 128–2095, http://dx.doi.org/10.1016/S0140-6736(12)61728-0.

[2] C. Yuan, S.-x. Zhang, N.L. Polissar, D. Echelard, G. Ortiz, J.W. Davis, E. Ellington, M.S. Ferguson, T.S. Hatsukami, Identification of fibrous cap rupture with magnetic resonance imaging is highly associated with recent transient ischemic attack or stroke, Circulation 105 (2) (2002) 181–185.

[3] E. Falk, Pathogenesis of atherosclerosis, J. Am. Coll. Cardiol. 47 (8 Suppl) (2006) C7–12, http://dx.doi.org/10.1016/j.jacc.2005.09.068.

[4] A.C. Akyildiz, L. Speelman, H.A. Nieuwstadt, H. van Brummelen, R. Virmani, A. van der Lugt, A.F. van der Steen, J.J. Wentzel, F.J. Gijsen, The effects of plaque morphology and material properties on peak cap stress in human coronary arteries, Comput. Methods Biomech. Biomed. Eng. 19 (7) (2016) 771–779.

[5] R. Virmani, A.V. Finn, F.D. Kolodgie, Carotid plaque stabilization and progression after stroke or TIA, 2009.

[6] T.G. Brott, J.L. Halperin, S. Abbara, J.M. Bacharach, J.D. Barr, R.L. Bush, C.U. Cates, M.A. Creager, S.B. Fowler, G. Friday, V.S. Hertzberg, E.B. McIff, W.S. Moore, P.D. Panagos, T.S. Riles, R.H. Rosenwasser, A.J. Taylor, 2011 ASA/ACCF/AHA/AANN/AANS/ACR/ASNR/CNS/SAIP/SCAI/SIR/SNIS/SVM/SVS guideline on the management of patients with extracranial carotid and vertebral artery disease: a report of the American college of cardiology foundation/American heart association task force on practice guidelines, and the American stroke association, American association of neuroscience nurses, American association of neurological surgeons, American college of radiology, American society of neuroradiology, congress of neurological surgeons, society of atherosclerosis imaging and prevention, society for cardiovascular angiography and interventions, society of interventional radiology, society of NeuroInterventional surgery, society for vascular medicine, and society for vascular surgery, J. Am. Coll. Cardiol. 57 (8) (2011) e16–94, http://dx.doi.org/10.1016/j.jacc.2010.11.006.

[7] G.C. Cheng, H.M. Loree, R.D. Kamm, M.C. Fishbein, R.T. Lee, Distribution of circumferential stress in ruptured and stable atherosclerotic lesions. a structural analysis with histopathological correlation, Circulation 87 (4) (1993) 1179–1187.

[8] A.C. Akyildiz, L. Speelman, H. van Brummelen, M.A. Gutiérrez, R. Virmani, A. van der Lugt, A.F. van der Steen, J.J. Wentzel, F.J. Gijsen, Effects of intima stiffness and plaque morphology on peak cap stress, Biomed. Eng. Online 10 (2011) 1–13.

[9] A. Veress, J.F. Cornhill, K.A. Powell, E. Herderick, J. Thomas, Finite element modeling of atherosclerotic plaque, Proc. Comput. Cardiol. Conf. (1993) 791–794.

[10] R.T. Lee, A.J. Grodzinsky, E.H. Frank, R.D. Kamm, F.J. Schoen, Structure-dependent dynamic mechanical behavior of fibrous caps from human atherosclerotic plaques, Circulation 83 (5) (1991) 1764–1770.

[11] C.-K. Chai, A.C. Akyildiz, L. Speelman, F.J. Gijsen, C.W. Oomens, M.R. van Sambeek, A. van der Lugt, F.P. Baaijens, Local anisotropic mechanical properties of human carotid atherosclerotic plaques–characterisation by micro-indentation and inverse finite element analysis, J. Mech. Behav. Biomed. Mater. 43 (2015) 59–68.

[12] H.M. Loree, A.J. Grodzinsky, S.Y. Park, L.J. Gibson, R.T. Lee, Static circumferential tangential modulus of human atherosclerotic tissue, J. Biomech. 27 (2) (1994) 195–204.

[13] R.A. Baldewsing, J.A. Schaar, F. Mastik, C.W. Oomens, A.F. van der Steen, Assessment of vulnerable plaque composition by matching the deformation of a parametric plaque model to measured plaque deformation, IEEE Trans. Med. Imaging 24 (4) (2005) 514–528.

[14] S. Barrett, M. Sutcliffe, S. Howarth, Z.-Y. Li, J. Gillard, Experimental measurement of the mechanical properties of carotid atherothrombotic plaque fibrous cap, J. Biomech. 42 (11) (2009) 1650–1655.

[15] D.M. Ebenstein, D. Coughlin, J. Chapman, C. Li, L.A. Pruitt, Nanomechanical properties of calcification, fibrous tissue, and hematoma from atherosclerotic plaques, J. Biomed. Mater. Res. Part A: An Official J. Soc. Biomater. Jpn. Soc. for Biomater. Australian Soc. Biomater. the Korean Soc. Biomater. 91 (4) (2009) 1028–1037.

[16] E. Maher, A. Creane, S. Sultan, N. Hynes, C. Lally, D.J. Kelly, Tensile and compressive properties of fresh human carotid atherosclerotic plaques, J. Biomech. 42 (16) (2009) 2760–2767.

[17] M.G. Lawlor, M.R. O'Donnell, B.M. O'Connell, M.T. Walsh, Experimental determination of circumferential properties of fresh carotid artery plaques, J. Biomech. 44 (9) (2011) 1709–1715.

[18] E. Maher, A. Creane, S. Sultan, N. Hynes, C. Lally, D.J. Kelly, Inelasticity of human carotid atherosclerotic plaque, Ann. Biomed. Eng. 39 (2011) 2445–2455.

[19] M.H. Kural, M. Cai, D. Tang, T. Gwyther, J. Zheng, K.L. Billiar, Planar biaxial characterization of diseased human coronary and carotid arteries for computational modeling, J. Biomech. 45 (5) (2012) 790–798.

[20] V.M. Heiland, C. Forsell, J. Roy, U. Hedin, T.C. Gasser, Identification of carotid plaque tissue properties using an experimental–numerical approach, J. Mech. Behav. Biomed. Mater. 27 (2013) 226–238.

[21] A. Karimi, M. Navidbakhsh, A. Shojaei, S. Faghihi, Measurement of the uniaxial mechanical properties of healthy and atherosclerotic human coronary arteries, Mater. Sci. Eng.: C 33 (5) (2013) 2550–2554.

[22] C.-K. Chai, A.C. Akyildiz, L. Speelman, F.J. Gijsen, C.W. Oomens, M.R. van Sambeek, A. van der Lugt, F.P. Baaijens, Local axial compressive mechanical properties of human carotid atherosclerotic plaques—characterisation by indentation test and inverse finite element analysis, J. Biomech. 46 (10) (2013) 1759–1766.

[23] A.V. Kamenskiy, I.I. Pipinos, Y.A. Dzenis, C.S. Lomneth, S.A.J. Kazmi, N.Y. Phillips, J.N. MacTaggart, Passive biaxial mechanical properties and in vivo axial pre-stretch of the diseased human femoropopliteal and tibial arteries, Acta Biomater. 10 (3) (2014) 1301–1313.

[24] Z. Teng, Y. Zhang, Y. Huang, J. Feng, J. Yuan, Q. Lu, M.P. Sutcliffe, A.J. Brown, Z. Jing, J.H. Gillard, Material properties of components in human carotid atherosclerotic plaques: a uniaxial extension study, Acta Biomater. 10 (12) (2014) 5055–5063.

[25] E.M. Cunnane, J.J. Mulvihill, H.E. Barrett, M.T. Walsh, Simulation of human atherosclerotic femoral plaque tissue: the influence of plaque material model on numerical results, Biomed. Eng. Online 14 (2015) 1–12.

[26] A. Karimi, M. Navidbakhsh, A. Shojaei, A combination of histological analyses and uniaxial tensile tests to determine the material coefficients of the healthy and atherosclerotic human coronary arteries, Tissue Cell 47 (2) (2015) 152–158.

[27] M.A. Jankowska, M. Bartkowiak-Jowsa, R. Bedzinski, Experimental and constitutive modeling approaches for a study of biomechanical properties of human coronary arteries, J. Mech. Behav. Biomed. Mater. 50 (2015) 1–12.

[28] L.A. Davis, S.E. Stewart, C.G. Carsten III, B.A. Snyder, M.A. Sutton, S.M. Lessner, Characterization of fracture behavior of human atherosclerotic fibrous caps using a miniature single edge notched tensile test, Acta Biomater. 43 (2016) 101–111.

[29] A. Karimi, S.M. Rahmati, T. Sera, S. Kudo, M. Navidbakhsh, A combination of constitutive damage model and artificial neural networks to characterize the mechanical properties of the healthy and atherosclerotic human coronary arteries, Artif. Organs. 41 (9) (2017) E103–E117.

[30] M. Kobielarz, M. Kozuń, A. Kuzan, K. Maksymowicz, W. Witkiewicz, C. Pezowicz, The intima with early atherosclerotic lesions is load-bearing component of human thoracic aorta, Biocybern. Biomed. Eng. 37 (1) (2017) 35–43.

[31] A.C. Akyildiz, L. Speelman, F.J. Gijsen, Mechanical properties of human atherosclerotic intima tissue, J. Biomech. 47 (4) (2014) 773–783.

[32] S. Avril, M. Bonnet, A.-S. Bretelle, M. Grédiac, F. Hild, P. Ienny, F. Latourte, D. Lemosse, S. Pagano, E. Pagnacco, Overview of identification methods of mechanical parameters based on full-field measurements, Exp. Mech. 48 (2008) 381–402.

[33] A.C. Akyildiz, H.H. Hansen, H.A. Nieuwstadt, L. Speelman, C.L. De Korte, A.F. van der Steen, F.J. Gijsen, A framework for local mechanical characterization of atherosclerotic plaques: combination of ultrasound displacement imaging and inverse finite element analysis, Ann. Biomed. Eng. 44 (2016) 968–979.

[34] S. Guvenir Torun, H.M. Torun, H.H. Hansen, G. Gandini, I. Berselli, V. Codazzi, C.L. De Korte, A.F. Van der Steen, F. Migliavacca, C. Chiastra, Multicomponent mechanical characterization of atherosclerotic human coronary arteries: an experimental and computational hybrid approach, Front. Physiol. 12 (2021) 733009.

[35] S.G. Torun, H.M. Torun, H.H. Hansen, C.L. de Korte, A.F. van der Steen, F.J. Gijsen, A.C. Akyildiz, Multicomponent material property characterization of atherosclerotic human carotid arteries through a Bayesian optimization based inverse finite element approach, J. Mech. Behav. Biomed. Mater. 126 (2022) 104996.

[36] F. Pierron, M. Grédiac, The Virtual Fields Method: Extracting Constitutive Mechanical Parameters from Full-Field Deformation Measurements, Springer Science & Business Media, 2012.

[37] T. Nguyen, J.M. Huntley, I.A. Ashcroft, P.D. Ruiz, F. Pierron, A Fourier-series-based virtual fields method for the identification of three-dimensional stiffness distributions and its application to incompressible materials, Strain 53 (5) (2017) e12229.

[38] J.H. Kim, S. Avril, A. Duprey, J.P. Favre, Experimental characterization of rupture in human aortic aneurysms using a full-field measurement technique, Biomech Model. Mechanobiol 11 (6) (2012) 841–853, http://dx.doi.org/10.1007/s10237-011-0356-5.

[39] S. Avril, P. Badel, A. Duprey, Anisotropic and hyperelastic identification of in vitro human arteries from full-field optical measurements, J. Biomech. 43 (15) (2010) 2978–2985.

[40] M.R. Bersi, V.A. Acosta Santamaría, K. Marback, P. Di Achille, E.H. Phillips, C.J. Goergen, J.D. Humphrey, S. Avril, Multimodality imaging-based characterization of regional material properties in a murine model of aortic dissection, Sci. Rep. 10 (1) (2020) 9244.

[41] F. Pierron, M. Grédiac, Towards material testing 2.0. a review of test design for identification of constitutive parameters from full-field measurements, Strain 57 (1) (2021) e12370, http://dx.doi.org/10.1111/str.12370.

[42] R.W. Boekhoven, M.F. Peters, M.C. Rutten, M.R. van Sambeek, F.N. van de Vosse, R.G. Lopata, Inflation and bi-axial tensile testing of healthy porcine carotid arteries, Ultrasound Med. Biol. 42 (2) (2016) 574–585, http://dx.doi.org/10.1016/j.ultrasmedbio.2015.09.019.

[43] R.W. Boekhoven, M.C.M. Rutten, M.R. van Sambeek, F.N. van de Vosse, R.G.P. Lopata, Towards mechanical characterization of intact endarterectomy samples of carotid arteries during inflation using Echo-CT, J. Biomech. 47 (4) (2014) 805–814, http://dx.doi.org/10.1016/j.jbiomech.2014.01.016.

[44] M. Grediac, F. Pierron, S. Avril, E. Toussaint, The virtual fields method for extracting constitutive parameters from full-field measurements: a review, Strain 42 (4) (2006) 233–253.

[45] S. Avril, M. Grédiac, F. Pierron, Sensitivity of the virtual fields method to noisy data, Comput. Mech. 34 (2004) 439–452.

[46] A. Zaman, G. Helft, S. Worthley, J. Badimon, The role of plaque rupture and thrombosis in coronary artery disease, Atherosclerosis 149 (2) (2000) 251–266.

[47] F.J. Gijsen, B. Vis, H.E. Barrett, A.A. Zadpoor, H.J. Verhagen, D. Bos, A.F. Van Der Steen, A.C. Akyildiz, Morphometric and mechanical analyses of calcifications and fibrous plaque tissue in carotid arteries for plaque rupture risk assessment, IEEE Trans. Biomed. Eng. 68 (4) (2020) 1429–1438.

[48] M. Wong, J. Edelstein, J. Wollman, M.G. Bond, Ultrasonic-pathological comparison of the human arterial wall. verification of intima-media thickness, Arter. Thromb.: A J. Vasc. Biology 13 (4) (1993) 482–486.

[49] H. Nieuwstadt, S. Fekkes, H. Hansen, C. de Korte, A. van der Lugt, J. Wentzel, A. van der Steen, F. Gijsen, Carotid plaque elasticity estimation using ultrasound elastography, MRI, and inverse FEA–A numerical feasibility study, Med. Eng. Phys. 37 (8) (2015) 801–807.

[50] C.L. de Korte, H.H. Hansen, A.F. van der Steen, Vascular ultrasound for atherosclerosis imaging, Interface Focus. 1 (4) (2011) 565–575.

[51] J.E. Wilhjelm, M.-L. Gronholdt, B. Wiebe, S.K. Jespersen, L.K. Hansen, H. Sillesen, Quantitative analysis of ultrasound B-mode images of carotid atherosclerotic plaque: correlation with visual classification and histological examination, IEEE Trans. Med. Imaging 17 (6) (1998) 910–922.

[52] H. Hansen, R. Lopata, T. Idzenga, C.L. de Korte, Full 2D displacement vector and strain tensor estimation for superficial tissue using beam-steered ultrasound imaging, Phys. Med. Biol. 55 (11) (2010) 3201.

[53] H.H. Hansen, R.G. Lopata, M. Keijts, T. Idzenga, C.L. de Korte, Noninvasive strain imaging in pulsating vessels using beam steered ultrasound acquisitions, in: 2011 IEEE International Symposium on Biomedical Imaging: From Nano To Macro, IEEE, 2011, pp. 1078–1081.

[54] B. Narayanan, M.L. Olender, D. Marlevi, E.R. Edelman, F.R. Nezami, An inverse method for mechanical characterization of heterogeneous diseased arteries using intravascular imaging, Sci Rep 11 (1) (2021) 22540, http://dx.doi.org/10.1038/s41598-021-01874-3.

[55] A.T. Latorre, M.A. Martinez, E. Pena, Characterizing atherosclerotic tissues: in silico analysis of mechanical properties using intravascular ultrasound and inverse finite element methods, Front. Bioeng Biotechnol 11 (2023) 1304278, http://dx.doi.org/10.3389/fbioe.2023.1304278.

[56] S. Pabi, M. Khan, S.K. Jain, A.K. Sen, A. Raj, et al., Effect of stenotic shapes and arterial wall elasticity on the hemodynamics, Phys. Fluids 35 (10) (2023).

[57] Y. Sun, J. Huang, Q. Lu, X. Yue, X. Huang, W. He, Y. Shi, J. Liu, Modeling fibrous tissue in vascular fluid–structure interaction: A morphology-based pipeline and biomechanical significance, Int. J. Numer. Methods Biomed. Eng. 41 (1) (2025) e3892.

[58] T.M. Morrison, G. Choi, C.K. Zarins, C.A. Taylor, Circumferential and longitudinal cyclic strain of the human thoracic aorta: age-related changes, J. Vasc. Surg. 49 (4) (2009) 1029–1036.

[59] E. Widman, K. Caidahl, B. Heyde, J. D'hooge, M. Larsson, Ultrasound speckle tracking strain estimation of in vivo carotid artery plaque with in vitro sonomicrometry validation, Ultrasound Med. Biol. 41 (1) (2015) 77–88.

[60] J. Ohayon, O. Dubreuil, P. Tracqui, S. Le Floc'h, G. Rioufol, L. Chalabreysse, F. Thivolet, R.I. Pettigrew, G. Finet, Influence of residual stress/strain on the biomechanical stability of vulnerable coronary plaques: potential impact for evaluating the risk of plaque rupture, Am. J. Physiology-Heart Circ. Physiol. 293 (3) (2007) H1987–H1996.

[61] L. Speelman, A. Akyildiz, B. Den Adel, J. Wentzel, A. Van der Steen, R. Virmani, L. Van der Weerd, J.W. Jukema, R. Poelmann, E. Van Brummelen, et al., Initial stress in biomechanical models of atherosclerotic plaques, J. Biomech. 44 (13) (2011) 2376–2382.

[62] J. Bols, J. Degroote, B. Trachet, B. Verhegghe, P. Segers, J. Vierendeels, A computational method to assess the in vivo stresses and unloaded configuration of patient-specific blood vessels, J. Comput. Appl. Math. 246 (2013) 10–17.